Clays and Clay Minerals

A multi-technique characterisation of cronstedtite synthetized by iron-clay interaction in a step by step cooling procedure

--Manuscript Draft--

Manuscript Number:	CCM-748R1
Full Title:	A multi-technique characterisation of cronstedtite synthetized by iron-clay interaction in a step by step cooling procedure
Short Title:	Synthesis of cronstedtite by iron-clay interaction
Article Type:	Article
Section/Category:	
Keywords:	Cronstedtite; MDO polytypes; radioactive waste storage; experimental iron-clay interaction.
Corresponding Author:	Isabella Pignatelli GeoRessources Vandœuvre-lès-Nancy, FRANCE
Corresponding Author Secondary Information:	
Corresponding Author's Institution:	GeoRessources
Corresponding Author's Secondary Institution:	
First Author:	Isabella Pignatelli
First Author Secondary Information:	
Order of Authors:	Isabella Pignatelli
	Enrico Mugnaioli, doctoral degree
	Jiri Hybler, doctoral degree
	Régine Mosser-Ruck, doctoral degree
	Michel Cathelineau, professor
	Nicolas Michau, doctoral degree
Order of Authors Secondary Information:	
Abstract:	The cooling of steel containers in radioactive waste storages has been simulated by an original step by step experiment from 90°C to 40°C. Among newly formed clay minerals observed in run products, cronstedtite has been undoubtedly identified by different analytical techniques (XRD, TEM and SEM). This is the first time that cronstedtite is so abundant and well-crystallized in an iron-clay interaction experiment. The supersaturation of experimental solutions with respect to cronstedtite is due to the availability of Fe and Si in solution, as a result of the dissolution of iron metal powder, quartz and in a minor amount other silicates. Cronstedtite crystals are characterized by various morphologies: pyramidal (truncated or not) with a triangular base and conic with a rounded or hexagonal cross-section. The pyramidal crystals occur more frequently and their polytypes (2M1, 1M, 3T) have been identified by selected area electron diffraction (SAED) patterns and by automated diffraction tomography (ADT). Cronstedtite is stable within the 90°-60°C temperature range. At temperature ≤ 50°C, cronstedite crystals show evidences of alteration.

Powered by Editorial Manager® and Preprint Manager® from Aries Systems Corporation

Manuscript
Click here to download Manuscript: Pignatelli_etal._modified.doc

A MULTI-TECHNIQUE CHARACTERISATION OF CRONSTEDTITE SYNTHETIZED BY IRON-CLAY INTERACTION IN A STEP BY STEP COOLING PROCEDURE

I. Pignatelli[a,*], E. Mugnaioli[b], J. Hybler[c], R. Mosser-Ruck[a], M. Cathelineau[a], N. Michau[d]

[a]. GeoRessources UMR-CRNS 7359, Université de Lorraine, Faculté des sciences et technologies, Campus Aiguillettes, BP 70239, 54506 Vandœuvre-lès-Nancy, France

[b]. Institut für Physikalische Chemie, Johannes Gutenberg-Universität Mainz, Welderweg 11, 55128 Mainz, Germany

[c]. Institute of Physics, Academy of Science of Czech Republic, Cukrovarnicka 10, 16253 Prague 6, Czech Republic

[d]. Agence nationale pour la gestion des déchets radioactifs (ANDRA), Direction Recherche et Développement/Service Colis et Matériaux, Parc de la Croix Blanche, 1/7 rue Jean Monnet, 92298 Châtenay-Malabry Cedex, France

* Corresponding Author: Isabella Pignatelli

Email: isabella.pignatelli@univ-lorraine.fr

Tel: +33 (0)3 83 68 47 28

Fax: +33 (0)3 83 68 47 01

ABSTRACT

The cooling of steel containers in radioactive waste storages was simulated by an original step by step experiment from 90°C to 40°C. Among newly formed clay minerals observed in run products, cronstedtite was undoubtedly identified by different analytical techniques (powder XRD, TEM and SEM). This is the first time that cronstedtite is so abundant and well-

crystallized in an iron-clay interaction experiment. The supersaturation of experimental solutions with respect to cronstedtite is due to the availability of Fe and Si in solution, as a result of the dissolution of iron metal powder, quartz and in a minor amount other silicates. Cronstedtite crystals are characterized by various morphologies: pyramidal (truncated or not) with a triangular base and conic with a rounded or hexagonal cross-section. The pyramidal crystals occur more frequently and their polytypes ($2M_1$, $1M$, $3T$) were identified by selected area electron diffraction (SAED) patterns and by automated diffraction tomography (ADT). Cronstedtite is stable within the 90°-60°C temperature range. At temperature ≤ 50°C, cronstedite crystals show evidences of alteration.

KEYWORDS

Cronstedtite, MDO polytypes, radioactive waste storage, experimental iron-clay interaction.

INTRODUCTION

This paper presents a multi-technique characterization of cronstedtite crystals formed from an original experimental procedure on iron-clay interactions. The choice of this experiment was driven by the need to evaluate the effects of a progressive decrease in temperature expected during the cooling of nuclear waste containers. First of all, a mineralogical assemblage was obtained after heating at 90°C an iron-clay mixture. Its retrograde evolution was thus simulated by a step by step cooling experiment between 90°C and 40°C. For the first time, single crystals of well-crystallized cronstedtite were observed in run products and accurately characterized. The temperature stability domain of cronstedtite was estimated on the basis of experimental evidence (occurrence and instability of crystals) and compared to literature data. This detailed mineralogical characterization of newly formed cronstedtite is useful to improve databases of the thermodynamic models.

BACKGROUND

Cronstedtite is a T-O or 1:1 phyllosilicate, with a general formula $(Fe^{2+}_{3-x}\ Fe^{3+}_{x})(Si_{2-x}Fe^{3+}_{x})O_5(OH)_4$, with $0 < x < 0.8$ (Geiger *et al*., 1983; Smrčok *et al*., 1994; Hybler *et al*., 2000; Hybler *et al.*, 2002; Kogure *et al.*, 2002), close to the initial ideal formula $(Fe^{2+}_2\ Fe^{3+})(SiFe^{3+})O_5(OH)_4$ proposed by Hendricks (1939). Chemical analyses of cronstedtite also show that the octahedrally coordinated iron can be replaced by other cations as Mg^{2+}, Mn^{2+}, Al^{3+} (Frondel, 1962; Geiger *et al*., 1983) and that the tetrahedral sites can also contain Al^{3+} (Geiger *et al*., 1983; Hybler *et al*., 2002). Cronstedtite forms a solid solution with greenalite $(Fe^{2+}, Fe^{3+}, Mg, \square)_3(Si, Al)_2O_5(OH)_4$ (Guggenheim *et al*., 1982), another Fe-rich layer silicate, from which it differs by the presence of ferric iron in tetrahedral coordination.

Like other trioctahedral T-O phyllosilicates, standard polytypes of cronstedtite can be classified in four subfamilies, identical with Bailey's (1969) groups: A (1*M*, $2M_1$, 3*T* polytypes), B (2*O*, $2M_2$, 6*H*), C (1*T*, 2*T*, 3*R*) and D ($2H_1$, $2H_2$, 6*R*), on the basis of the interlayer shift and of the rotation between succeeding layers (Bailey, 1969). In the Order-Disorder theory (Dornberger-Schiff and Ďurovič, 1975) these polytypes are defined as *MDO* polytypes (Maximum Degree Order). Among them, only 8 polytypes have been reported for cronstedtite in the literature (Table 1): 1*T*, 1*M*, $2H_1$, $2H_2$, $2M_1$, 2*T*, 3*T* and 6*R* (Steadman and Nuttall, 1963, 1964). One non-standard or non-MDO polytype has also been found by Frondel (1962) in a cronstedtite sample coming from the Cornucopia mine (Nye Country, Nevada) and it was indicated by the Ramsdell symbol 9*R*.

In terrestrial environments, cronstedtite was found in sulfide veins as a low-temperature hydrothermal mineral, associated with siderite, pyrite, sphalerite and quartz (Frondel, 1962) and also in metamorphosed massive sulphide deposits (Lopez-Garcia *et al.*, 1992). In australian banded iron-formations of lower metamorphic grade, Gole (1980 a, b) reported the coexistence of greenalite with another mineral that he identified as probable cronstedtite.

Cronstedtite occurs also in carbonaceous chondrites both in fine-grained rims and matrices as product of aqueous alteration on the parent body (Müller *et al*., 1979; Barber, 1981; Burbine and Burns, 1994, Browning *et al*., 1996; Lauretta *et al*., 2000; Zega and Buseck, 2003; Miyahara *et al*., 2008)

A few experimental works reported the formation of T-O Fe-rich minerals of the serpentine group. Odinite (R^{3+}, R^{2+}, □)$_3$(Si_{2-x} Al_x)O_5(OH)$_4$ and hexagonal crystals of cronstedtite as run products of dioctahedral smectites-iron metal interactions at 80° C were reported by Lantenois (2003), Lantenois *et al.* (2005) and Lanson *et al*. (2012). Under similar experimental conditions, Fe-rich T-O phyllosilicates were described as "berthierine type" phases with general formula (R^{2+}, R^{3+}, □)$_3$(Si_{2-x}, Al_x)O_5(OH)$_4$ (Brindley, 1982) or "Fe-rich 7 Å clays" or "serpentine-like minerals" (Wilson *et al*., 2006; Perronnet *et al*., 2007; Mosser-Ruck *et al*., 2010; Jodin-Caumon *et al*., 2010; de Combarieu *et al.*, 2011; Jodin-Caumon *et al*., 2012; Rivard *et al*., 2013), sometimes close to the greenalite end-member (Pierron, 2011). The numerous designations of low temperature Fe-rich phyllosilicates found in literature were explained by the difficulty of their identification. They often appeared as highly disordered or nanocristallines phases (Schlegel *et al*., 2008) or as small crystal associated with Si-Al-Fe gels (Perronnet *et al*., 2008), and they can coexisted with other Fe-rich phases in experimental run products.

MATERIALS AND METHODS

Starting material

The starting clay rich rock used in our experiments is a claystone from the Callovo-Oxfordian formation (noted COx) of the Paris Basin, a formation investigated for future waste storage in the underground research laboratory (URL) at the Meuse/Haute-Marne site of Bure (France). The claystone contains on average 41% of clay minerals (illite, mixed-layered illite/smectite,

being the predominant clay minerals, and minor amounts of kaolinite and chlorite), 25% of quartz, 31% of carbonates (calcite and minor dolomite) and the remaining 3% consist of pyrite, phosphates, K-feldspar and organic matter (Rousset, 2002; Gaucher *et al.*, 2004).

The starting products (experimental solutions and clays) were prepared under inert argon atmosphere, using a solution of 0.0207 mol/kg NaCl and 0.0038 mol/kg $CaCl_2$ (pH = 6.4) and 1 g of claystone grinded in a mortar to obtain a liquid/solid mass ratio of 10. Metal iron was added to the system as a powder (500 mg; average grain size ~ 40 µm) and as two plates with dimensions of nearly $3x6x1mm^3$ (iron powder/COx mass ratio of 0.5). The starting mixture was put in Parr® non-stirred pressure vessels made of Teflon® with capacity of ~20 ml. Seven vessels were heated in a furnace at 90(±2)° C for 6 months and then the temperature was decreased every month by steps of 10°C until 40°C. At each temperature, a vessel was removed from the oven. After quenching and opening of each vessel, the solid run products were dried under an argon flux at room temperature.

ManoCalcimeter

Quantitative analysis of carbonates was performed in the Museum National d'Histoire Naturelle (MNHN) using a Mélières manoCalcimeter (MCM) on 200 mg of bulk rock sample powder (see Ledésert et al., 2009). MCM uses a "Karbonat-Bombe" which is a simple apparatus composed of glass flask and a high precision manometer (Dunn, 1980). This method gives a direct measurement of carbonates for rocks containing only calcite or aragonite ($CaCO_3$). The MCM is built to give a 100 mg value when 1 millimole of CO_2 is emitted during chemical attack of 100 mg (# 1 millimole) of $CaCO_3$ by 8N hydrochloric acid. Nevertheless, molecular weight of carbonates varying with their chemical composition and 100 mg of pure dolomite for example provokes the emission of 1.085 millimole of CO_2. As a consequence, the values read on the MCM must be corrected as a function of the amount of

the different carbonates identified by XRD. Calibration was performed using pure calcite crystals; uncertainty precision is around 0.5 wt.%.

X-ray diffraction

The data were collected at room temperature with a D8 Bruker diffractometer, using the CoKα radiation (λ = 1.7902 Å), 35kV accelerating voltage and 45mA intensity. The Bruker DIFFRAC^{plus} package was used for the data acquisition and analysis.

XRD patterns of randomly oriented powder were obtained, using a scan step of 0.035° (2θ), exposure time of 3 seconds, $2\theta_{min}$ = 3° and $2\theta_{max}$ = 54°**.**

Scanning electron microscopy (SEM)

The secondary electron (SE) and backscattered electrons (BSE) images of the cronstedtite crystals were obtained with an accelerating voltage of 15 kV using a cold FEG Hitachi S-4800. The lateral resolution of FEG-SEM is about 1 nm for SE images. The crystals of cronstedtite analysed were collected on the iron plates, deposited on the carbon adhesive sticks and then carbon coated. Energy dispersive X-ray spectra (EDXS) were performed to identify the chemical elements present in crystals.

Transmission electron microscopy (TEM) and Energy-dispersive X-ray (EDX) spectroscopy

TEM images and EDX analyses were carried out at 200 kV using a Philips CM20 microscope with a point resolution of 0.27 nm equipped with Si-Li detector. The TEM specimens were prepared dispersing the < 2 μm fraction powders in ethanol under ultrasonic and evaporing a drop of the suspension on a carbon network-like holey support film placed on a 200 mesh copper grid (Euromedex-Mundolcheim, France). The chemical composition of run products was determined using energy dispersive X-Ray spectroscopy (EDXS). EDX spectra were

recorded by means of a PGT spectrometer mounted on CM20 Philips microscope operated at 200 kV and equipped with an ultrathin window X-Ray detector. The analyses were carried out in nanoprobe mode with a probe diameter of 10 nm using K_{AB} determined from clay standards with similar thickness.

Selected area electron diffraction (SAED) patterns were recorded at 120 kV using a Philips CM120 microscope with a Digistar Nanomegas CCD camera.

Automated electron diffraction tomography (ADT)

3D electron diffraction data were also collected by a Tecnai F30 S-Twin microscope operating at 300 kV. Powdered sample (< 2 µm fraction) was dispersed in ethanol, sonified and sprayed on a carbon-coated copper grid by a UIS250v Hielscher sonifier, according to the procedure described by Mugnaioli *et al.* (2009). Data collection was carried out by a combination of automated diffraction tomography (ADT) and precession electron diffraction (PED) (Kolb *et al*., 2007, 2008; Mugnaioli *et al*., 2009). Nano electron diffraction patterns were collected in steps of 1° in a tilt range up to -60/+60°. Data processing, 3D reciprocal space reconstruction and cell parameter determination were performed by ADT3D software.

Analysis of solutions

The pH of each run solution was measured with a combination of silver/sulfide electrode in glove box after cooling at room temperature and 0.025 µm filtration. The electrode was calibrated using reference buffer solutions certified by PTB and NIST Institutes with pH 4, 7 and 10. The run solutions were diluted ten times in 2% vol. HNO_3 and analyzed by inductively coupled plasma optical emission spectroscopy (ICP-OES) at LIMOS laboratory to determine the concentration of dissolved Si and Fe.

RESULTS

ManoCalcimeter and X-ray diffraction

XRD patterns of untreated mixed iron-COx sample and run samples are shown in Figure 1. Calcite reflection at 3.03 Å is unchanged on the 90°C to 40°C patterns, indicating that this mineral is unaffected by the cooling. As the manoCalcimeter results confirm that calcite content is constant (10±1 wt%) in all samples, XRD patterns were normalized to calcite reflection (3.03 Å). Intensities of quartz, iron metal and T-O-T phyllosilicates (mica and illite) reflections decrease on XRD pattern of 90°C experiment. This decrease is emphasized on the other XRD patterns corresponding to 80°C-40°C experiments. At the same time, intensities of magnetite and 7 Å phyllosilicates increase. This indicates a strong dissolution of quartz and iron metal (more than 70% for both phases) and partial destruction of T-O-T phyllosilicate layers. The XRD results highlight the increase of the 7 Å clays amount in run products but don not allow to accurately distinguish T-O minerals because of their similar d_{hkl}.values.

Scanning electron microscopy

The SEM analyses show that dominant 7 Å clays obtained in the 90°C experiment are iron-rich and have different morphologies (Figure 2). Pyramidal (truncated or not) crystal with a triangular base and conic crystals were observed. The last ones have rounded or hexagonal cross-sections (Figure 2a-b). The different morphologies still coexist down to 70° C (Figure 2c-d), then at lower temperatures pyramidal shape becomes the dominant morphology (Figure 2e-f).

Transmission electron microscopy

Energy dispersive X-ray analyses and TEM imaging

EDX analyses were performed on isolated particles of < 2 µm fraction powders. From the EDX results, structural formulae have been calculated on the basis of 7 oxygens and the Fe^{3+}/Fe^{2+} ratio has been adjusted to set the occupation of the octahedral sites to 3. The compositions (expressed as a.p.f.u., *i.e.* atom per formula unit) of 28 pyramidal crystals and 5 conic crystals formed at 90° and 80° C are reported in Tables 2 and 3. The mean formula is:

$$(Fe^{2+}_{2.2}Fe^{3+}_{0.8})(Si_{1.2}Al_{0.1}Fe^{3+}_{0.7})O_5(OH)_4$$

The difference in the chemistry of crystals with respect to their morphology is not significant considering the standard deviation (Tables 2 and 3). The Si-deficit and the presence of ferric iron in the tetrahedral sites allow to identify these two types of crystals as cronstedtite.

TEM images show that the higher crystallinity of the newly formed iron rich clays was observed in 70°C and 60°C run products (Figure 3) and also that this mineral becomes unstable at temperature ≤ 50°C as demonstrated by alteration of its faces (Figure 4). At 40°C very rare relict crystals of altered cronstedtite were still observed.

SAED patterns and ADT/PED investigations: determination of cronstedtite polytypes

Because of their great abundance in run product, well-shaped pyramidal cronstedtites formed during 70°C experiment were chosen to identify their MDO polytypes following the procedure described by Ďurovič (1981). According to the Order-Disorder (OD) theory (Dornberger-Schiff, 1956, 1964, 1966, and 1979), the superposition vectors and rotations (of almost identical 1:1 layers) needed to obtain the four possible subfamily structures, are as follows: $\pm\mathbf{a}_i/3$ for subfamily A; $\pm\mathbf{b}/3$ or zero for subfamily C; $\pm\mathbf{a}_i/3$, and $\pm\mathbf{b}/3$ or zero combined with 180º rotation for subfamilies B and D, respectively (Dornberger-Schiff, 1964; Bailey, 1969). The $\mathbf{a}_i$ and $\mathbf{b}$ are hexagonal and orthohexagonal unit cell vectors, respectively.

It follows that the subfamily sublattice corresponding to the Fourier transform of subfamily structure is formed by reflections with $k = 3n$ (in orthohexagonal indexing, or $h\text{-}k = 3n$ in

hexagonal indexing). These reflections are common to all polytypes belonging to the same subfamily and are consequently called *subfamily reflections*. Whereas the reflection having $k \neq 3n$ (in orthohexagonal indexing, or $h\text{-}k \neq 3n$ in hexagonal indexing) are typical of each polytypes and are said *non-family* or *polytype reflections*. Usually diffraction patterns of two orthogonal reciprocal lattice sections are enough to identify a MDO polytype: the diffraction pattern of ($h0l$)* (*hhl* in hexagonal indexing) containing the subfamily reflections allowing to determine the subfamily and the diffraction pattern from ($0kl$)* ($\bar{h}hl$ in hexagonal indexing), containing both subfamily and polytype reflection useful to identify the polytype (Ďurovič, 1997). In non-trigonal and non-hexagonal poytypes, however, the diffraction pattern of the ($0kl$)* plane is different from that of ($h0l$)*, because they are not symmetry equivalent (Ďurovič, priv. comm.). In order to determine such polytypes to a certainty the ($0kl$)* planes should be recorded and checked as well.

The spots distribution on experimental electron diffraction 2D patterns were compared with the identification diagrams for MDO polytypes of cronstedtite described in literature (Ďurovič, 1997, Hybler *et al.*, 2008), and with diffraction patterns theoretically calculated with aid of the DIFK91 program (Smrčok and Weiss, 1993).

SAED patterns of several pyramidal cronstedtites underline that they are all 1*M* polytypes. The spot distribution along the 11*l* reciprocal lattice row on (hhl_{hex})* plane indicates that these crystals belong to the subfamily (Bailey's group) A (Figure 5). Moreover the spot distribution on ($h0l_{\text{hex}}$)* and ($0kl_{\text{hex}}$)* planes corresponds to MDO group II and I respectively (Figure 6). Both are in agreement with theoretically calculated patterns. 1*M* cronstedtite polytype is very rare and generally occurs intergrown to the 3*T* polytype and strongly disordered (Ďurovič, 1997).

Three ADT data sets were collected on different crystals and reconstructed in 3D diffraction volumes. The first acquisition, coming from a nicely shaped pyramidal crystal (Figure 7a),

247 shows diffuse scattering along c^* for both $h0l_{hex}$ and hhl_{hex} reflections, so that no polytypic
248 identification can be made (Figure 7b).
249 The second acquisition comes from a crystal with pyramidal shape, where two corners are
250 truncated and one not (Figure 8a). Remarkably the not-truncated corner is characterized by
251 diffuse disorder, while the rest of the crystal delivers a mostly coherent diffraction consistent
252 with the subfamily A and to MDO group III, *i.e.* $2M_1$ polytype (Figure 8b-d). The cell is *C*-
253 centred monoclinic with parameters a = 5.5 Å, b = 9.6 Å, c = 14.4 Å, β = 97.4°. Systematic
254 absences for reflections $h0l$ with $l \neq 2n$ suggest the presence of a glide plane c perpendicular
255 to the b axis. This is in agreement with the space group *Cc* found by Steadman and Nuttall
256 (1964) for this polytype. Worth noting is that $2M_1$ polytype of cronstedtite is also very rare in
257 nature (Ďurovič, 1997). The presence of diffuse scattering along c^* testifies anyway to a
258 certain degree of disorder even in most ordered parts of the crystal.
259 The third acquisition highlights the presence of another polytype belonging to the subfamily
260 A and MDO group IV, *i.e.* 3*T* polytype (Figure 9a-b). The cell is hexagonal with parameters a
261 = 5.5 Å, and c = 21.4 Å. Intensity distribution suggests a trigonal symmetry (Laue class $P\bar{3}$
262 or $P\bar{3}1m$), consistent with the space group $P3_1$ reported in literature (Steadman and Nuttall,
263 1963; Smrčok *et al.*, 1994).
264
265 *Solution chemistry*
266 The characterization of run solutions shows that the mean pH value is 7.47±0.16 and that Si
267 concentration varies between 7 and 11 ppm in function of the experiments (Figure 10). Quartz
268 solubility at each run temperature has been calculated by PHREEQC geochemical software
269 package V2.17 (Parkhurst and Appelo, 1999) and the associated LLNL database (Johnson et
270 al., 2000). Si concentration is under the quartz solubility curve in run solution of experiment
271 carried out in the temperature range of 90°-60° C, whereas at 50° C the Si concentration is on

the quartz solubility curve. Finally, the Si concentration slightly increases in the last run solution (40° C). Fe concentration in the experimental solutions is very low (< 1 ppm) or under limit detection.

DISCUSSION AND CONCLUSIONS

The significant decrease of quartz, T-O-T phyllosilicates and iron metal intensity reflections on X-ray diffraction patterns indicates that these phases were dissolved releasing Si and Fe in experimental solutions. Quartz dissolution is confirmed by Si concentration measured in run solutions which is lower than that at equilibrium with quartz between 90°-60°C (Figure 10). At this temperature range, cronstedtite is formed together with other 7 Å clays. As iron content in run solutions is lower than 1 ppm or under limit of detection (< 5 ppb), it is all incorporated in newly formed minerals (cronstedtite, magnetite and other iron-rich silicates). At temperatures of 50° and 40°C measured Si content is respectively equal and higher than that at equilibrium with quartz, preventing the precipitation of cronstedtite. Thanks to the original step by step cooling procedure presented in this paper, the stability range of cronstedtite with respect to the temperature was determined. Between 90°C to 60°C cronstedtite appears to be stable and 50°C corresponds to the lower limit of cronstedtite stability as confirmed by crystal alteration (Results §). The upper limit is ≥ 90°C but it cannot be accurately determined. Surely, no cronstedtite has ever been observed in similar experiments carried out on the same claystone (COx) at higher temperatures of 150°C and 300°C (Pierron, 2011).

The cooling experiments from 90°C to 60°C favored the development of crystals with pyramidal (truncated or not) morphologies and enhanced crystallinity. Pyramidal crystals analyzed by TEM show different polytypic sequences and various degrees of disorder. The identified polytypes, all belonging to the subfamily A, are $2M_1$ and $1M$ together with $3T$.

297 According to Hybler *et al.* (2008), these two monoclinic polytypes are very rare whereas 3*T*
298 polytype is relatively abundant in nature. The mean formula for pyramidal polytypes is in
299 good agreement with that reported by Kogure *et al*. (2002) for cronstedtite of subfamily A,
300 even if our crystals contain small amounts of Al and Mg (Table 2). Conic crystals of
301 cronstedtite occur with pyramidal ones only in 90°C and 80°C experiments. The coexistence
302 of these two different morphologies may be due to changes of the supersaturation degree
303 during growth. When the supersaturation decreased, the crystals take a polyhedral habitus
304 bounded by flat faces (Sunagawa, 2005), changing the morphology from conic to pyramidal.
305 According to the literature, one can also suppose that conic crystals may be cronstedtite
306 polytypes belonging to the C or D subfamilies (Frondel, 1962; Kogure *et al*., 2001; Hybler *et*
307 *al*., 2002). The co-occurrence of one of these two subfamilies with the subfamily A has been
308 already observed (C + A or D + A subfamilies) by Hybler *et al*. (2008). The detailed study of
309 conic crystals is the object of an investigation under development and will be discussed in a
310 future work.
311
312 *Comparison with cronstedtite from chondrites*
313 Several studies about the formation conditions of cronstedtite were carried out on
314 carbonaceous chondrites in which this mineral is the dominant component (Dyl *et al*., 2010).
315 Cronstedtite crystals in meteorites are often small, platy and characterized by high degree of
316 stacking disorder (Müller *et al*., 1979; Lauretta *et al*., 2000; Zega and Buseck., 2003). For this
317 reason it is difficult to identify their polytypes. Nevertheless, Müller *et al*. (1979) and Zaga
318 and Buseck (2003) found mostly 1*T* polytype and Müller *et al*. (1979) reported that the
319 second more frequent polytype is 1*M*. Even if the conditions of cronstedtite formation in
320 meteorites are close to those of our experiments (presence of metal Fe, neutral-alkaline
321 solution, reducing conditions), 1*T* polytype was not observed in our run products. Mass-

transfer and reaction-path calculations simulating aqueous alteration in chondrites propose that the upper limit of cronstedtite stability is 90°-100°C according to Schulte and Shock (2004) and McAlister and Kettler (2008). These calculations were done with the hypothesis that the activity of silica in solution is close to quartz saturation. This disagrees with our chemical data obtained on experimental solution which indicate that the activity of aqueous silica is under quartz saturation between 90°C and 70°C.

Comparison with run products in similar experimental conditions

The results presented in this paper have shown that the occurrence of cronstedtite is restricted to the 90°C-50°C domain of temperature. But at 90°C, in the 6 months experiment, cronstedtite is not so abundant and its crystallinity degree is low. Is it a kinetic or temperature effect? To answer this question, our results were compared to those of similar experiments carried out on the same starting materials. Rivard (2011) and Pierron (2011) used the same claystone (COx of the Meuse/Haute-Marne site of Bure) at 90°C for 9 months but using slightly different liquid/solid mass ratio (20 and 10 respectively) and iron powder/COx mass ratio (0.2 and 0.1 or 1 respectively). They observed the crystallization of iron-rich T-O clays with a composition between odinite, berthierine and greenalite (Figure 11). No cronstedtite have been reported by these authors. These results seem to confirm that the formation of cronstedtite is strongly favored by a lower temperature range, and maybe by a temperature decrease.

Concluding remarks

In clay formations which may be host deep-geological radioactive waste disposal, a first increase of temperature to 90° C close to the containers and then followed by a cooling is expected. Our experiments simulated the mineralogical evolution of the iron-clay system

around the steel containers during a cooling between 90° and 40° C. They showed that the composition of iron rich T-O clays stable at 90°C (close to odinite, greenalite or berthierine) will evolve toward cronstedtite during the cooling. This result has to be taken into account in the understanding of complex interaction in glass-iron-clay systems.

ACKNOWLEDGMENTS

The authors thank L. Mouton and J. Ghanbaja respectively for SEM and TEM images and analyses at SCMEM laboratory (Université de Lorraine, France). U. Kolb is warmly thanked for providing access to TEM laboratory at the Institut für Physikalische Chemie, Johannes Gutenberg Universität. The authors also wish to thank M. Klementova and L. Palatinus for acquisition and processing of SAED patterns, L. Truche for helpful discussion. This research was financially supported by ANDRA – Agence Nationale pour la gestion des Déchets Radioactifs (French national agency for the management of radioactive wastes).

REFERENCES

Bailey, S.W. (1969) Polytypism of trioctahedral 1:1 layer silicates. *Clays and Clay Minerals*, **17**, 355-371.

Bailey, S.W. (1988) Odinite, a new dioctahedral-trioctahedral Fe^{3+}-rich 1:1 clay mineral. *Clay Minerals*, **23**, 237-247.

Barber, D.J. (1981) Matrix phyllosilicates and associated minerals in C2M carbonaceous chondrites. *Geochimica et Cosmochimica Acta*, **45**, 945-970.

Brindley, G.W. (1982) Chemical compositions of berthierines – A review. *Clays and Clay Minerals*, **30**, 153-155.

Browning, L.B., McSween, H.Y. Jr. and Zolensky, M.E. (1996) Correlated alteration effects in CM carbonaceous chondrites. *Geochimica et Cosmochimica Acta*, **60**, 2621-2633.

Burbine, T.H. and Burns, R.G. (1994) Questions concerning the oxidation of the ferrous iron in carbonaceous chondrites. *Lunar Planetary Science*, **XXV**, 199-200.

de Combarieu, G., Schlegel, M.L., Neff, D., Foy, E. Vantelon, D., Barboux, P. and Gin, S. (2011) Glass-iron-clay interactions in a radioactive waste geological disposal : an integrated laboratory-scale experiment. *Applied Geochemistry*, **26**, 65-79.

Dornberger-Schiff, K. (1956) On Order-Disorder Structures (OD-Structures). *Acta Crystallographica*, **9**, 593-601.

Dornberger-Schiff, K. (1964) Grundzüge einer Theorie von OD-Strukturen aus Schichten. Abh. dtsch. Akad Wiss Berlin, Kl. f. Chem., 3, 107 p.

Dornberger-Schiff, K. (1966) Lehrgang üer OD-Strukturen. Berlin: Akademine-Verlag, 135 p.

Dornberger-Schiff, K. (1979) OD structures- a game and a bit more. *Kristall Und Technik*, **14**, 1027-1045.

Dornberger-Schiff, K. and Ďurovič, S. (1975) OD-interpretation of kaolinite-type structure-I: symmetry of kaolinite packets and their stacking possibilities. *Clays and Clay Minerals*, **23**, 219-229.

Dunn, D.A. (1980). Revised techniques for quantitative calcium carbonate analysis using the "Karbonat-Bombe," and comparisons to other quantitative carbonate analysis methods. *Journal of Sedimentary Research*, **50**, 631–636.

Ďurovič, S. (1981) OD-Charakter, Polytypie und Identifikation von Schichtsilikaten. *Fortschritte der Mineralogie*, **59**, 191-226.

Ďurovič, S. (1997) Cronstedtite-1*M* and co-existence of 1*M* and 3*T* polytypes. *Ceramics – Silikáty*, **41** (3), 98-104.

Dyl, K.A., Manning, C.E. and Young, E.D. (2010) The implication of the cronstedite in water-rich planetesimals and asteroids. Astrobiology Science Conference 2010, League City, Texas.

Frondel, C. (1962) Polytypism in cronstedtite. *American Mineralogist*, **47**, 781-783.

Gaucher, E., Robelin, C., Matray. J.M., Négrel, G., Gros, Y., Heitz, J.F., Vinsot, A., Rebours, H., Cassagnabère, A. and Bouchet, A. (2004) ANDRA underground research laboratory : interpretation of the mineralogical and geochemical data acquired in the Callovian-Oxfordian formation by investigative drilling. *Physics and Chemistry of the Earth*, **29**, 55-77.

Geiger, C.A., Henry, D.L., Bailey, S.W. and Maj, J.J. (1983) Crystal structure of cronstedtite-$2H_2$. *Clays and Clay Minerals*, **31**, 97-108.

Gole, M.J. (1980a) Low-temperature retrograde minerals in metamorphosed Archean banded iron-formations, Western Australia. *Canadian Mineralogist*, **18**, 205-214.

Gole, M.J. (1980b) Mineralogy and petrology of very-low metamorphic grade Archean banded iron-formations, Weld Range, Western Australia. *American Mineralogist*, **65**, 8-25.

Guggenheim, S., Bailey, S.W., Eggleton, R.A. and Wilkes, P. (1982) Structural aspects of greenalite and related minerals. *Canadian Mineralogist*, **20**, 1-18.

Hendricks, S.B. (1939) Random Structures of layer minerals as illustrated by cronstedtite ($2FeO{\cdot}Fe_2O_3{\cdot}SiO_2{\cdot}2H_2O$). Possible iron content of kaolin. *American Mineralogist*, **24**, 529-539.

Hybler, J., Ďurovič, S. and Kogure, T. (2008) Polytypism in cronstedtite. *Acta Crystallographica*, **A64**, C498-499.

Hybler, J., Petříček, V., Ďurovič, S. and Smrčok, L. (2000) Refinement of the crystal structure of cronstedtite-1*T*. *Clays and Clay Minerals*, **48**, 331-338.

Hybler, J., Petříček, V., Fábry, J. and Ďurovič, S. (2002) Refinement of the crystal structure of cronstedtite-2H_2. *Clays and Clay Minerals*, **50**, 601-613.

Jodin-Caumon, M.C., Mosser-Ruck, R., Randi, A., Pierron, O., Cathelineau, M. and Michau, N. (2012) Mineralogical evolutions of a claystone after reaction with iron under thermal gradient. *Clays and Clay Minerals*, **60**, 5, 443-455.

Jodin-Caumon, M.C., Mosser-Ruck, R**.**, Rousset, D., Randi, A., Cathelineau, M. and Michau, N. (2010) Effect of a thermal gradient on iron-clay interactions. *Clays and Clay Minerals*, **58**, 5, 667–681.

Johnson, L., Anderson, G., Parkhurst, D. (2000) Database from 'thermo.com.V8.R6.230' Prepared at Lawrence Livermore National Laboratory (Revision: 1.11).

Kogure, T., Hybler, J. and Ďurovič, S. (2001) A HRTEM study of cronstedtite : determination of polytypes and layer polarity in trioctahedral 1 :1 phyllosilicates. *Clays and Clay Minerals*, **49**, 310-317.

Kogure, T., Hybler, J. and Yoshida, H. (2002) Coexistence of two polytypic groups in cronstedtite from Lostwithiel England. *Clays and Clay Minerals*, **50**, 504-513.

Kolb, U., Gorelik, T. and Otten, M.T. (2008) Towards automated diffraction tomography. Part II – Cell parameter determination. *Ultramicroscopy*, 108, 763-772.

Kolb, U., Gorelik, T., Kübel, C. and Otten, M.T. (2007) Towards automated diffraction tomography : Part I – Data acquisition. *Ultramiscoscopy*, **107**, 507-513.

Lanson, B., Lantenois, S. Van Aken, P.A., Bauer, A. and Plançon, A. (2012) Experimental investigation of smectite interaction with metal iron at 80°C : structural characterization of newly formed Fe-rich phyllosilicates. *American Mineralogist*, **97**, 864-871.

Lantenois, S. (2003) Réactivié fer metal/smectites en milieu hydraté à 80°C, Ph.D. thesis, Université d'Orleans, Orleans, 220 pp.

444 Lantenois, S., Lanson, B., Muller, F., Bauer, A., Jullien, M. and Plançon, A. (2005)
445 Experimental study of smetite interaction with metal Fe at low temperature: 1. Smectite
446 destabilization. *Clays and Clay Minerals*, **53**, 597-612.
447 Lauretta, D.S., Hua, X. and Buseck, P.R. (2000) Mineralogy of fine-grained rims in the ALH
448 81002 CM chondrite. *Geochimica et Cosmochimica Acta*, **64**, 3263-3273.
449 Ledésert B., Hébert R., Grall C., Genter A., Dezayes C., Bartier D. and Gérard A. (2009).
450 Calcimetry as a useful tool for a better knowledge of flow pathways in the Soultz-sous-
451 Forêts Enhanced Geothermal System, *Journal of Volcanology and Geothermal Research*,
452 **181**, 106-114.
453 López García, J.A., Manteca, J.I., Prieto, A.C. and Calvo, B. (1992) Primera aparición en
454 España de cronstedtita. Caracterización estructural. *Boletín de la Sociedad Española de*
455 *Mineralogía*, **15-1**, 21-25.
456 McAlister, J.A. and Kettler, R.M. (2008) Metastable equilibria among dicarboxylic acids and
457 the oxidation state during acqueous alteration on the CM2 chondrite parent body.
458 *Geochimica et Cosmochimica Acta*, **72**, 233-241.
459 Miyahara, M., Uehara, S., Ohtani, E., Nagase T., Nishijima, M., Vashaei, Z. and Kitagawa, R.
460 (2008) The anatomy of altered chondrules and FGRs covering hem in a CM chondrite by
461 FIB-TEM-STEM. *Lunar Planetary Science*, **XXXIX**, 199-200.
462 Mosser-Ruck, R., Cathelineau, M., Guillaume, D. and Charpentier, D. (2010) Effects of
463 temperature, pH, and iron/clay and liquid7clay liquid/clay ratios on experimental
464 conversion of dioctahedral smectite to berthierine, chlorite, vermiculite, or saponite.
465 *Clays and Clay Minerals*, **58**, 280-291.
466 Mugnaioli, E., Gorelik, T. and Kolb, U. (2009) "Ab initio" structure solution from electron
467 diffraction data obtained by a combination of automated diffraction tomography and
468 precession technique. *UntramicroscopyUltramicroscopy*, **109**, 758-765.

Müller, W.F., Kurat, G. and Kracher, A. (1979) Chemical and crystallographic study of cronstedtite in the matrix of the Cochabamba (CM2) carbonaceous chondrite. *Tschermaks Mineralogische und Petrographische Mitteilungen*, **26**, 293-304.

Parkhurst, D.L., Appelo, C.A.J. (1999) User's guide to PHREEQC (Version 2). A Computer Program for Speciation, Batch-reaction, One-dimensional Transport, and Inverse Geochemical Calculations. U.S. Geological Survey Water-Resources Investigations Report 99-4259, 312 pp.

Perronnet, M., Jullien, M., Villiéras, F., Raynal, J., Bonnin, D. and Bruno, G. (2008) Evidence of a critical content in Fe(0) on FoCa7 bentonite reactivity at 80°C. *Applied Clay Science*, **38**, 187-202.

Perronnet, M., Villiéras, F., Jullien, M., Razafitianamaharavo, A., Raynal, J. and Bonnin, D. (2007) Towards a link between the energetic heterogeneities of the edge of smectites and their stability in the context of metallic corrosion. *Geochimica et Cosmochimica Acta*, **71**, 1463-1479.

Pierron, O. (2011) Interactions eau-fer-argilite : rôle des paramètres Liquide/Roche, Fer/Argilite, Température sur la nature des phases minérales, Ph.D. thesis, Université Henri Poincaré, Nancy, 226 pp.

Rivard, C. (2011) Contribution à l'étude de la stabilité des minéraux constitutifs de l'argilite du Callovo-Oxfordien en présence de fer à 90°C, Ph.D. thesis, Institut National Polytechnique de Lorraine, Nancy, 338 pp.

Rivard, C., Pelletier, M., Michau, N., Razafitianamaharavo, A., Bihannic, I., Abdelmoula, M., Ghanbaja, J. and Villiéras, F. (2013) Berthierine-like mineral formation and stability during the interaction of kaolinite with metallic iron at 90 °C under anoxic and oxic conditions. *American Mineralogist*, **98**, 163-180.

493 Rousset, D. (2002) Etude de la fraction argileuse de séquence sédimentaires de la Meuse et du
494 Gard. Reconstruction de l'histoire diagénetique et des caractéristiques physico-chimiques
495 des cibles, Ph.D. thesis, Université Louis Pasteur, Strasbourg, 269 pp.
496 Schlegel, M.L., Bataillon, C., Benhamida, K., Blanc, C., Menut, D. and Lacour, J. (2008)
497 Metal corrosion and argillite transformation at the water-saturated, high-temperature iron-
498 clay interface : a microscopic-scale study. *Applied Geochemistry*, **23**, 2619-2633.
499 Schulte, M. and Schock, E. (2004) Coupled organic synthesis and mineral alteration on the
500 meterorite parent bodies. *Meteoritic and Planetary Science*, **39**, 1577-1590.
501 Smrčok, L., Ďurovič, S., Petříček, V. and Weiss, Z. (1994) Refinement of the crystal structure
502 of cronstedtite-3*T*. *Clays and Clay Minerals*, **42**, 544-551.
503 Smrčok, L., Weiss, Z (1993) DIFK91: a program for the modelling of powder diffraction
504 patterns on a PC. Journal of Applied Crystallography 26, 140-141.
505 Steadman, R. and Nuttall, P.M. (1963) Polymorphism in cronstedtite. *Acta Crystallographica*,
506 **16**, 1-8.
507 Steadman, R. and Nuttall, P.M. (1964) Further polymorphism in cronstedtite. *Acta*
508 *Crystallographica*, **17**, 404-406.
509 Sunagawa, I. (2005) *Crystals. Growth, morphology and perfection*, Cambridge University
510 Press.
511 Wilson, J., Cressey G., Cressey, B., Cuadros, J., Vala Ragnarsdottir, K., Savage, D. and
512 Shibata, M. (2006) The effect of iron on montmorillonite stability. (II) Experimental
513 investigation. *Geochimica et Cosmochimica Acta*, **70**, 323-336.
514 Zega, T.J. and Buseck, P.R. (2003) Fine-grained-rim mineralogy of the Cold Bokkeveld CM
515 chondrite. *Geochimica et Cosmochimica Acta*, **67**, 1711-1721.
516
517

TABLES

Table 1. Polytypes of trioctahedral T-O phyllosilicates and cronstedtite (literature data).

Table 2. Cation contents (a.p.f.u, *i.e*. atom per formula unit) in 28 pyramidal crystals of cronstedtite formed between 90° and 80°C.

Table 3. Cation contents (a.p.f.u) in 5 conic crystals of cronstedtite formed between 90° and 80°C.

FIGURES CAPTIONS

Figure 1. XRD patterns of run samples collected from 90°C to 40°C experiments and untreated mixed iron-COx sample (Chl = chlorite, T-O-T Ph = T-O-T phyllosilicates, Qz = quartz).

Figure 2. a) SEM image of cronstedtite crystals with different morphologies in 90°C experiment and a relative EDX spectrum (b). c), d) BSE images of conic (in circle) and pyramidal cronstedtites in 70°C experiment. e), f) BSE and SE images of pyramidal crystals of cronstedtite in 60°C experiments.

Figure 3. TEM micrographs of conic (a, b) and pyramidal cronstedtites (c, d) formed between 90° and 80°C.

Figure 4. TEM image of unstable cronstedtite crystal in 50°C experiment.

Figure 5. SAED pattern of (hhl_{hex})* plane for 1*M* polytype. Note, that the pattern contains also few weak parasitic spots of an unidentified phase.

Figure 6. SAED patterns of ($h0l_{hex}$)* and ($0kl_{hex}$)* planes for 1*M* polytype.

Figure 7. First ADT acquisition. a) TEM image of the pyramidal crystal selected for ADT acquisition. b) ADT 3D diffraction reconstruction (along an oblique view) showing the diffuse scattering along *c**.

Figure 8. Second ADT acquisition. a) TEM image of the truncated crystal. The area pointed by the black arrow was affected by diffuse disorder, while the area pointed by the white arrow was selected for ADT acquisition. b) ADT 3D diffraction reconstruction viewed along *a**. White arrows point the reflections *h*0*l* with $l \neq 2n$ extinct due the *c*-glide plane. c) ADT 3D diffraction reconstruction viewed along *b**. d) ADT 3D diffraction reconstruction viewed along *c**. An extraneous reflection coming from another crystal is marked with a circle. Note that these are projections of a 3D diffraction volume and not conventional 2D electron diffraction patterns.

Figure 9. Third ADT acquisition. a) TEM image of the crystal selected for the acquisition (indicated by a black arrow). b) ADT 3D diffraction reconstruction viewed along *a** showing the 21.4 Å periodicity.

Figure 10. Si concentration (ppm) in run solutions *vs* experimental temperature.

Figure 11. Chemical composition of the most evolved newly formed T-O clays plotted in a Si-Al-Fetot ternary diagram. Experiments of this study are represented by diamonds. Pierron's experiments (2011) and Rivard's experiments (2011) are represented respectively by squares and triangles. Gr: greenalite $(Fe^{3+}_{0.45}Fe^{2+}_{1.9}Mg_{0.3}\square_{0.35})Si_{2.0}O_5(OH)_4$ (Guggenheim *et al*., 1982); Od: odinite $(Al_{0.15}Fe^{3+}_{1.2}Fe^{2+}_{0.35}Mg_{0.7}\square_{0.6})(Si_{1.85}Al_{0.15})O_5(OH)_4$ (Bailey, 1988); Be: berthierine $(Al_{0.96}Fe^{3+}_{0.22}Fe^{2+}_{1.49}Mg_{0.17}\square_{0.17})(Si_{1.15}Al_{0.85})O_5(OH)_4$ (Brindley, 1982); Cr: cronstedtite $(Fe^{3+}_{0.84}Fe^{2+}_{2.16})(Si_{1.16}Fe^{3+}_{0.84})O_5(OH)_4$ (Kogure *et al*., 2002).

Table 1

Polytypes of trioctahedral T-O phyllosilicates	***MDO polytypes of trioctahedral T-O phyllosilicates***				Authors
	A	B	C	D	Bailey (1969)
	1*M*, 2M_1, 3*T*	2*O*, 2M_2, 6*H*	1*T*, 2*T*, 3*R*	2H_1, 2H_2, 6*R*	
	MDO polytypes of cronstedtites				
	1*M*, 2M_1, 3*T*		1*T*, 2*T*	2H_1, 2H_2, 6*R*	Steadman and Nuttall, (1963, 1964)
Most frequent morphologies	Truncated trigonal pyramid shape, plates needles (3*T*)		Cones or trigonally deformed cones (1*T*)	Ovoïd based shape or columnar with rounded hexagonal or circular cross section (group D). Ovoid-to barrel-shaped morphology (2H_2)	Frondel, (1962); Hybler et al. (2000; 2002); Steadman and Nuttall, (1963); Kogure et al., (2001); Geiger et al. (1983)
Polytypes of trioctahedral T-O phyllosilicates	**Non-MDO polytypes of cronstedtites *:*** 9*R* Cornucopia mine (Nye Country, Nevada)				Frondel (1962)

577 **Table 2**

	Mg	Fe_{tot}	^{IV}Al	Si	^{IV}Fe	$^{VI}Fe^{2+}$	$^{VI}Fe^{3+}$
	0	3.79	0.02	1.19	0.79	2.18	0.81
	0.03	3.73	0.06	1.18	0.76	2.15	0.82
	0.02	3.68	0.09	1.20	0.70	2.18	0.80
	0	3.27	0.02	1.71	0.27	2.71	0.29
	0.10	3.54	0.19	1.17	0.64	2.07	0.83
	0.14	3.37	0.20	1.28	0.52	2.14	0.72
	0.03	3.71	0.11	1.15	0.74	2.12	0.88
	0.01	3.85	0.06	1.08	0.86	2.07	0.92
	0.01	3.73	0.04	1.22	0.74	2.21	0.78
	0.02	3.71	0.03	1.24	0.73	2.23	0.76
	0.01	3.81	0.02	1.16	0.82	2.15	0.84
	0	3.73	0.08	1.19	0.73	2.19	0.81
	0	3.89	0	1.11	0.89	2.11	0.89
	0.03	3.80	0.03	1.14	0.83	2.10	0.86
	0.07	3.35	0.27	1.31	0.42	2.24	0.70
	0	3.61	0.08	1.30	0.61	2.30	0.70
	0	3.84	0	1.16	0.84	2.16	0.84
	0.03	3.91	0.03	1.04	0.93	2.01	0.96
	0.06	3.59	0.10	1.25	0.65	2.19	0.75
	0	3.86	0	1.14	0.86	2.14	0.86
	0.04	3.89	0.03	1.04	0.93	2.00	0.96
	0.01	3.70	0.07	1.22	0.71	2.21	0.78
	0.02	3.82	0.07	1.10	0.84	2.08	0.90
	0.01	3.71	0.06	1.22	0.72	2.21	0.78
	0	3.77	0	1.23	0.77	2.23	0.77
	0	3.88	0	1.12	0.88	2.12	0.88
	0.01	3.76	0.05	1.18	0.77	2.18	0.82
	0.01	3.81	0.09	1.10	0.81	2.09	0.90
	0.06	3.27	0.28	1.38	0.33	2.32	0.61
Average	0.03	3.70	0.07	1.20	0.73	2.17	0.80
σ	0.03	0.18	0.08	0.13	0.16	0.13	0.13

578

579 **Table 3**

	Mg	Fe_{tot}	^{IV}Al	Si	^{IV}Fe	$^{VI}Fe^{2+}$	$^{VI}Fe^{3+}$
	0.01	3.74	0.07	1.18	0.75	2.17	0.82
	0.04	3.60	0.14	1.22	0.64	2.18	0.78
	0.04	3.59	0.15	1.21	0.63	2.17	0.79
	0.01	3.75	0.10	1.14	0.76	2.13	0.86
	0.04	3.53	0.26	1.17	0.58	2.12	0.84
Average	0.03	3.64	0.14	1.18	0.67	2.16	0.82
σ	0.02	0.10	0.07	0.03	0.08	0.03	0.03

580

Figure 1
Click here to download Figure: Figure 1.eps

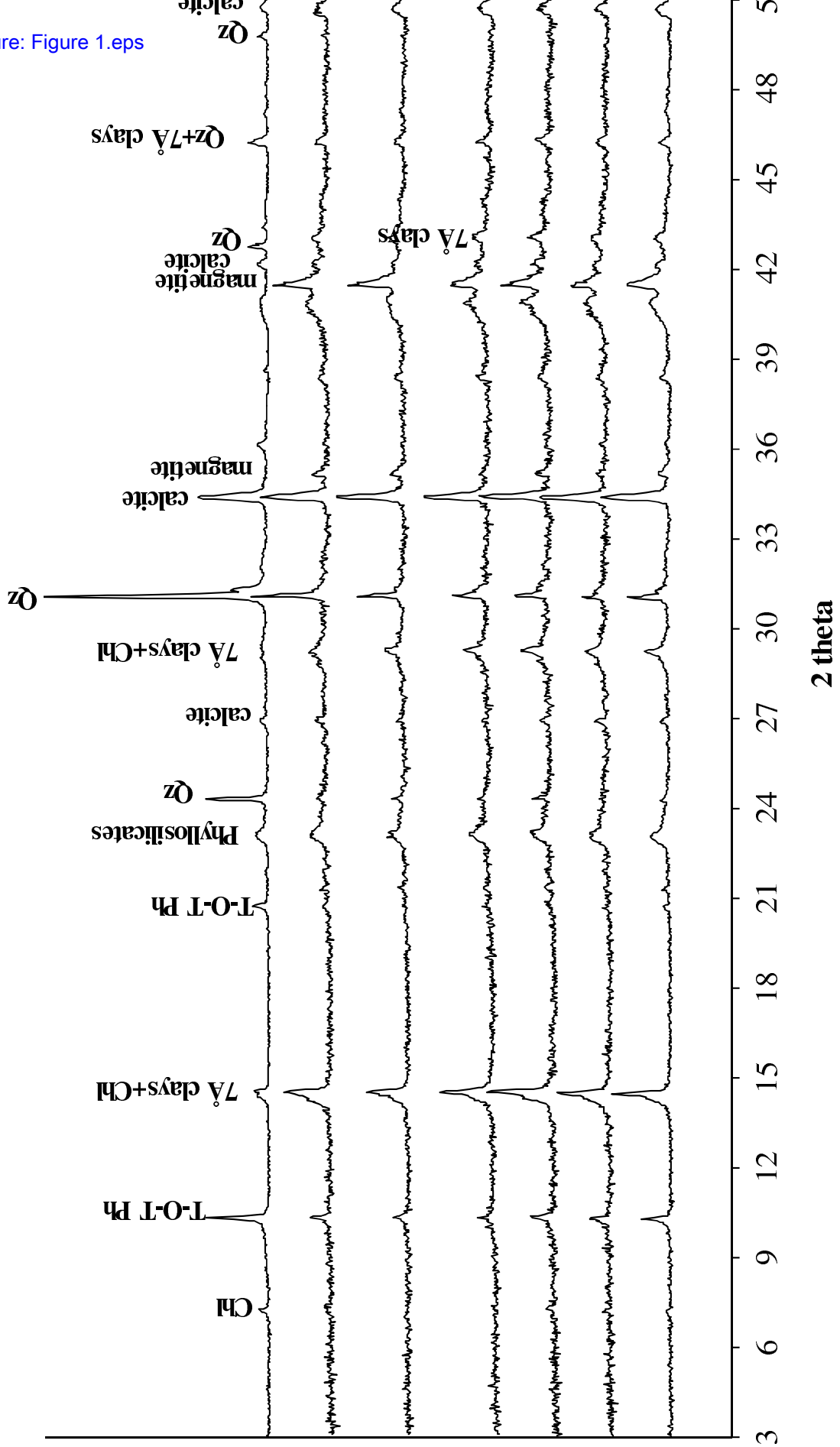
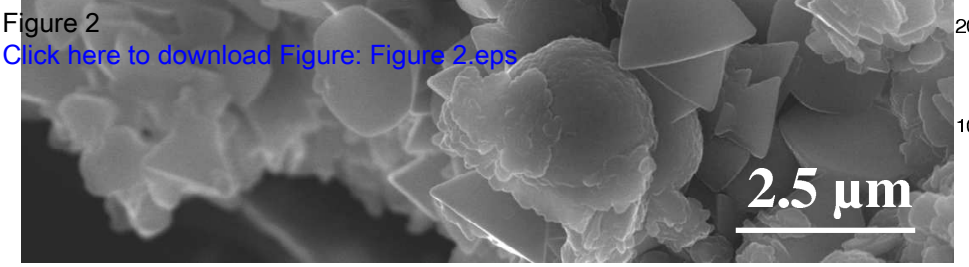
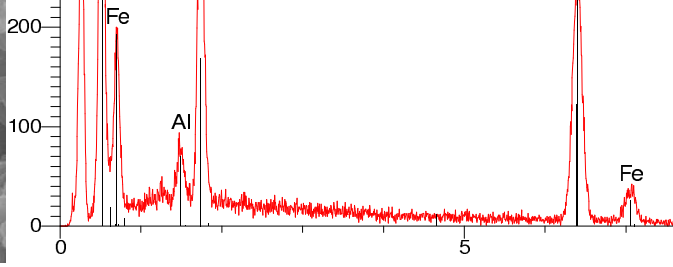
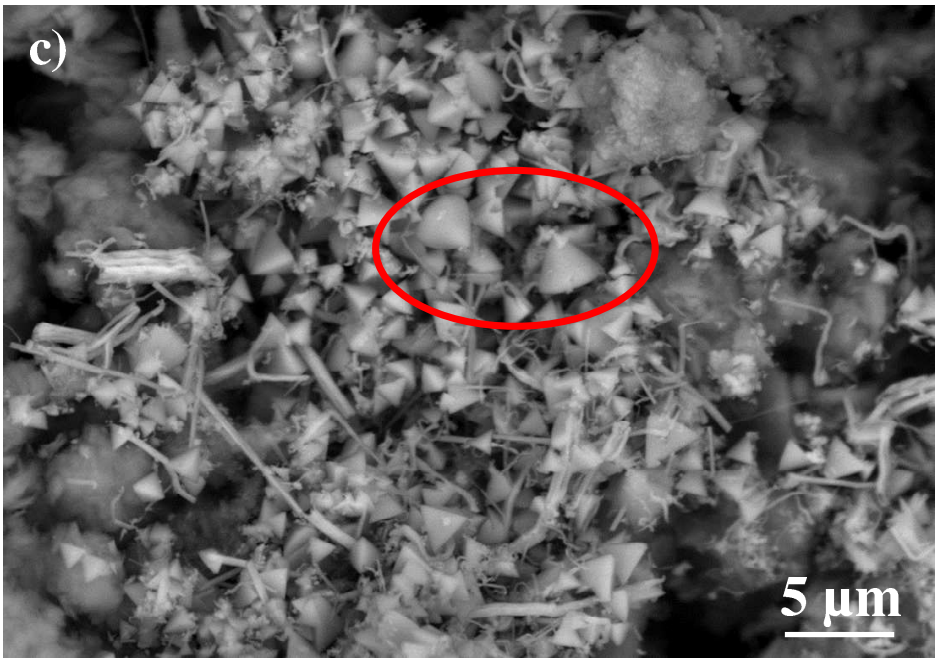
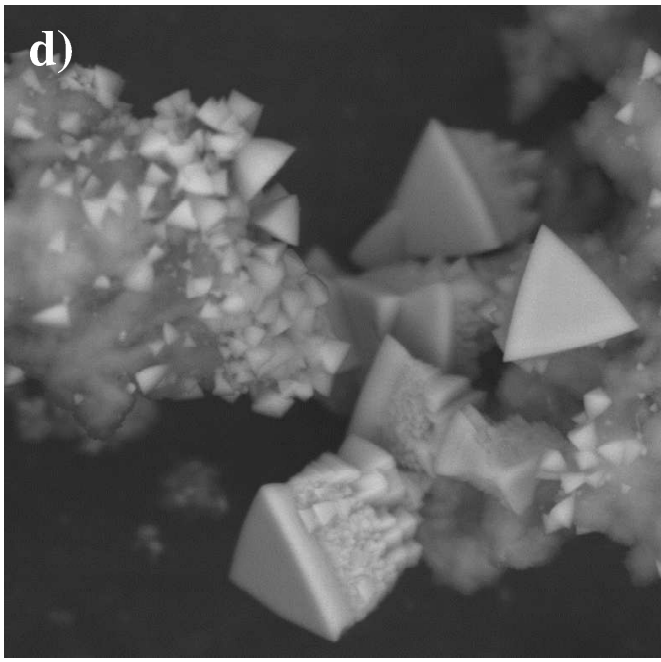


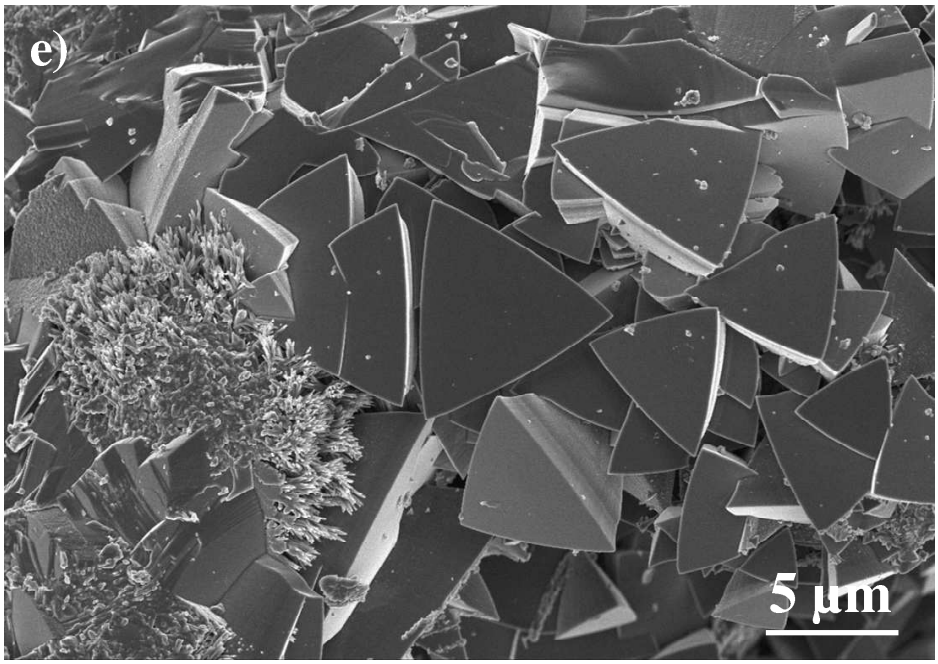
Figure 2
Click here to download Figure: Figure 2.eps











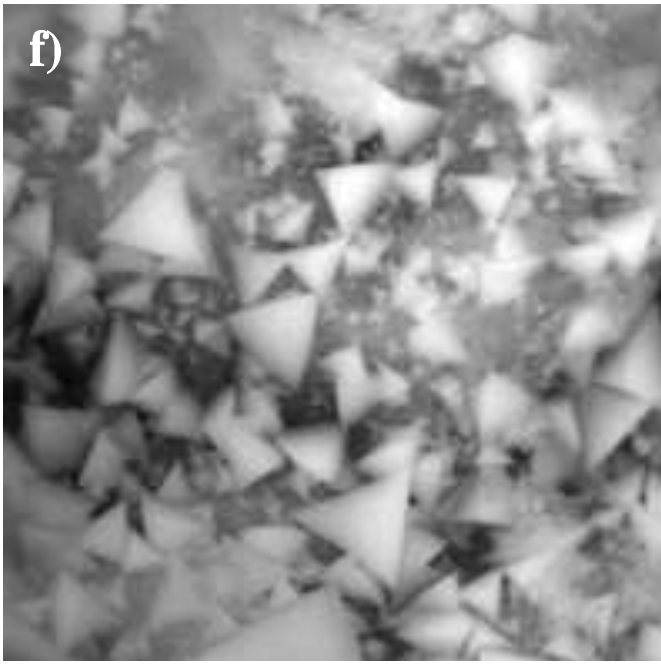


Figure 3
Click here to download Figure: Figure 3.eps

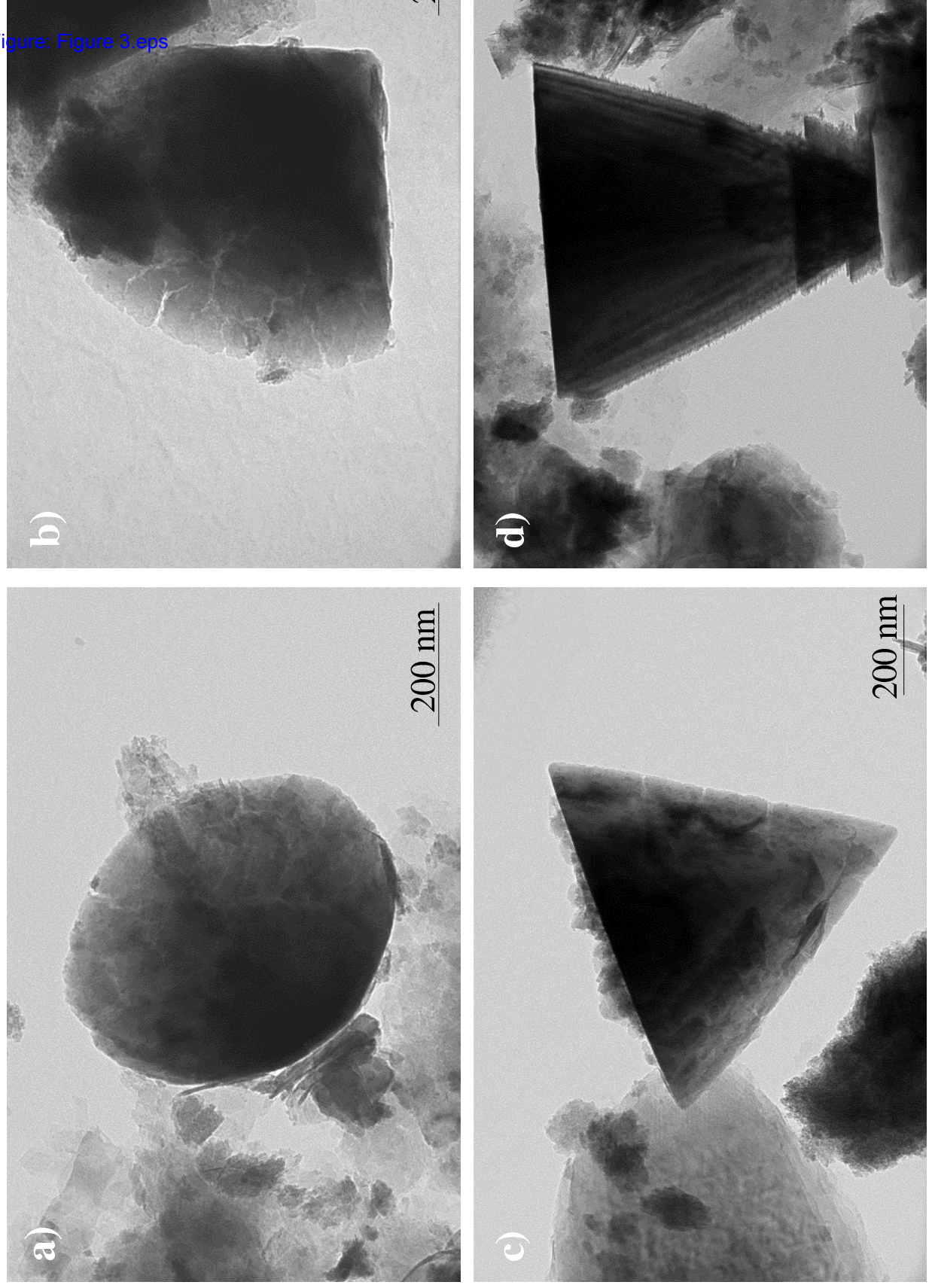


Figure 4
Click here to download Figure: Figure 4.eps

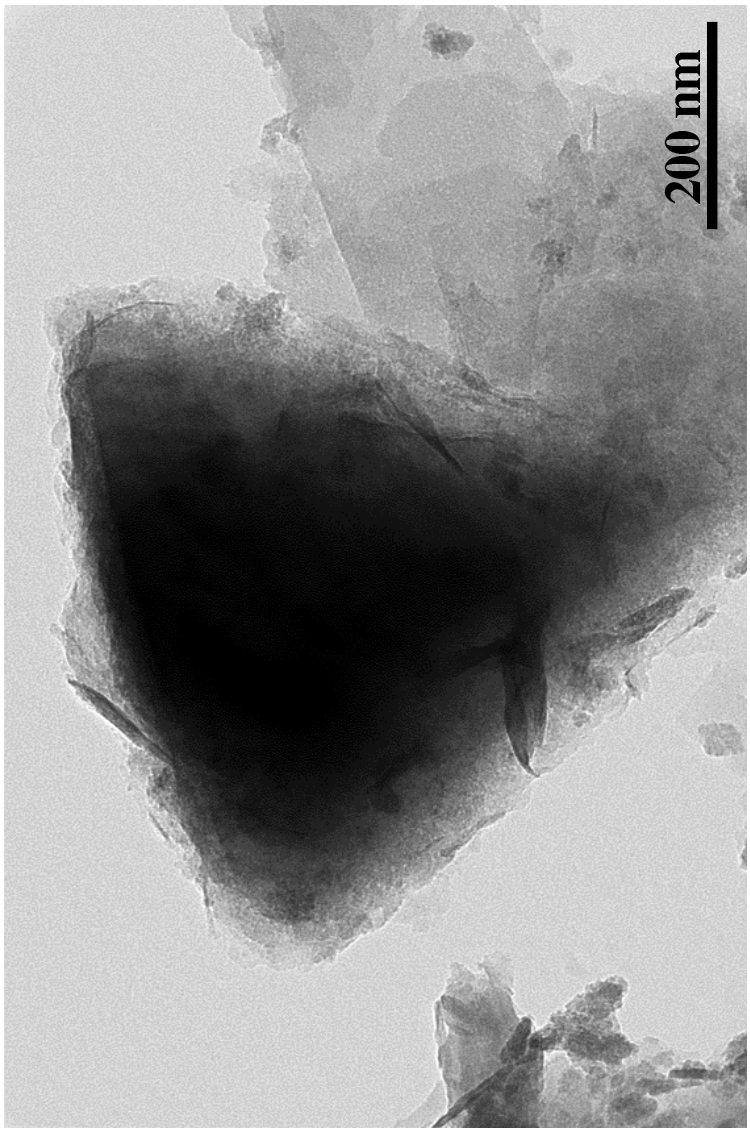


Figure 5
Click here to download Figure: Figure 5.eps

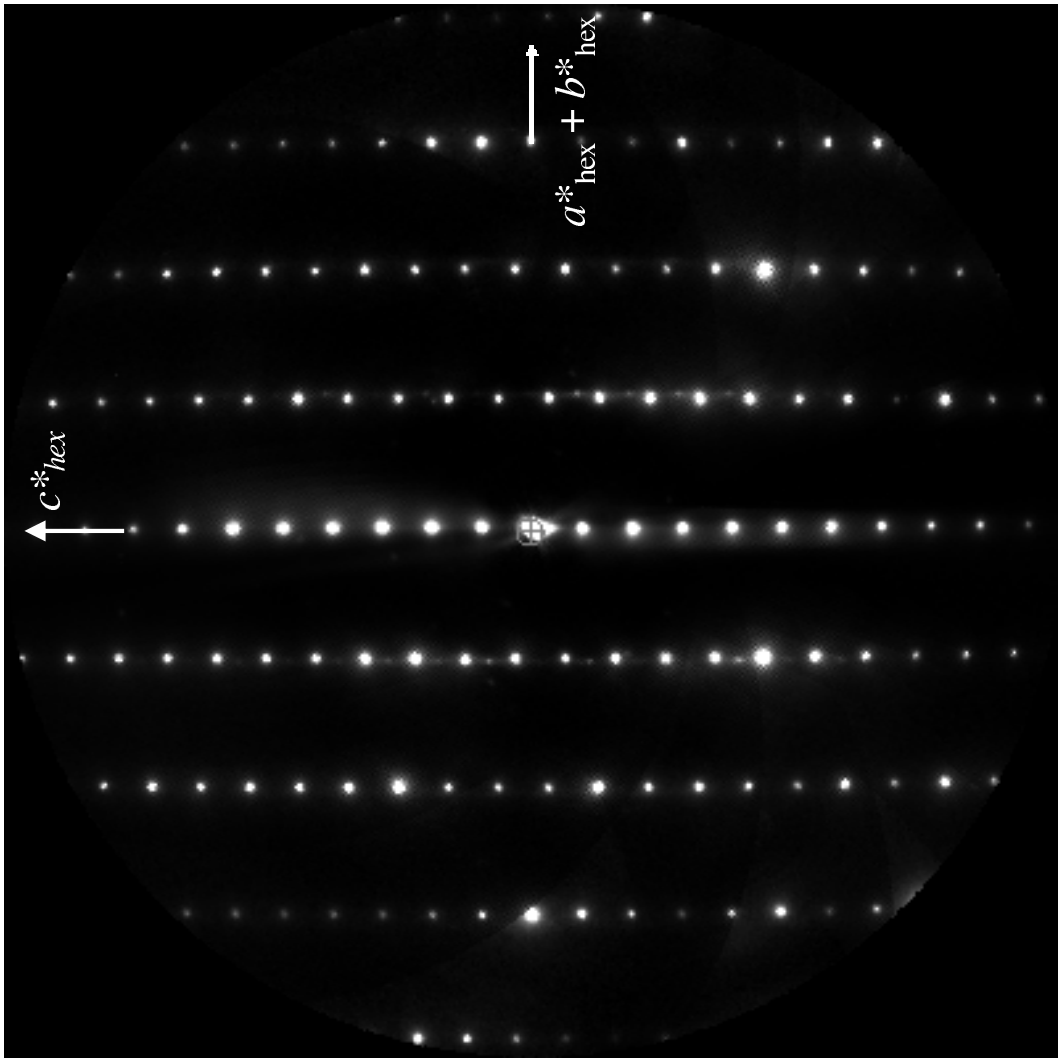


Figure 6
Click here to download Figure: Figure 6.eps

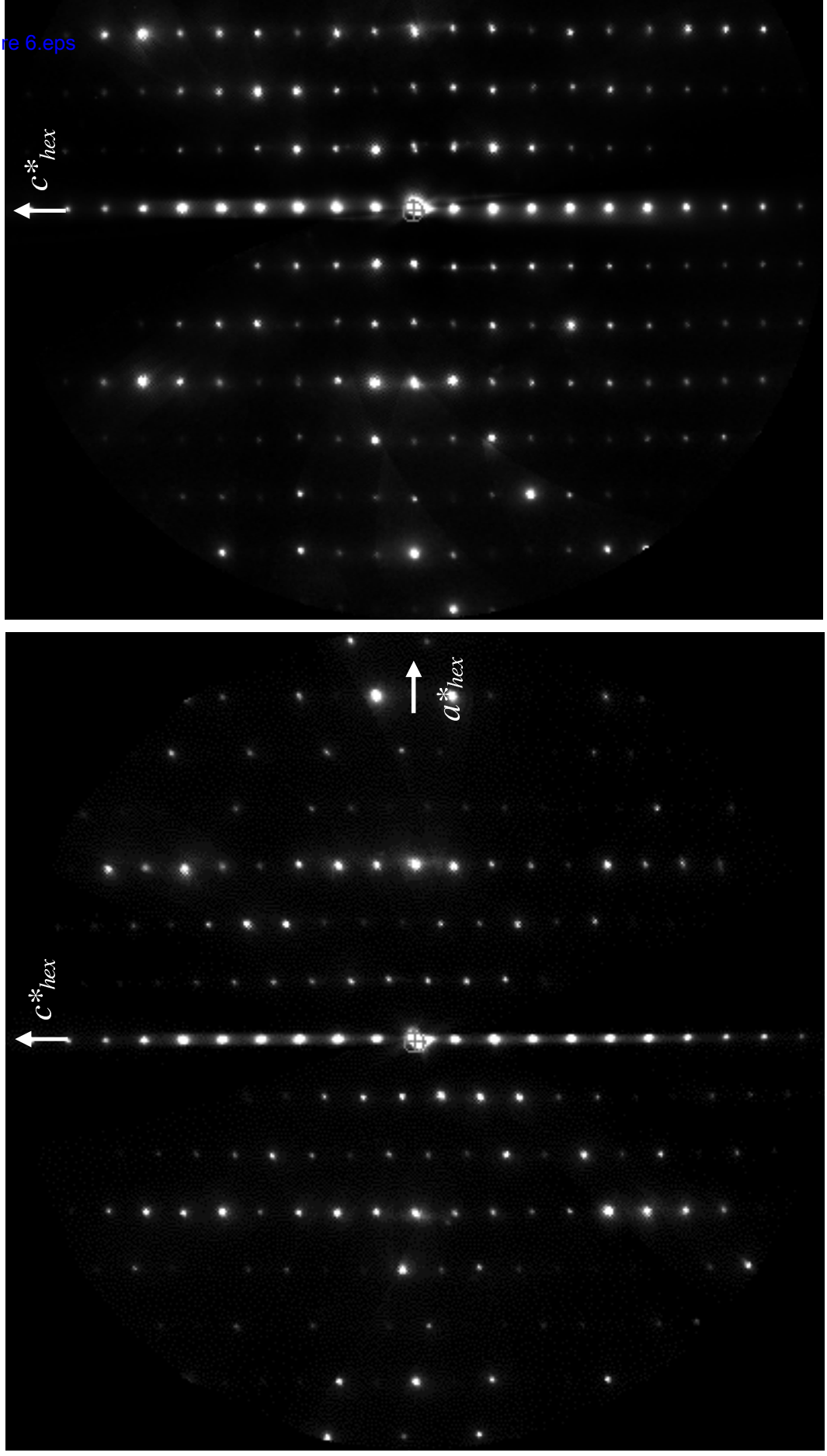


Figure 7
Click here to download Figure: Figure 7.eps

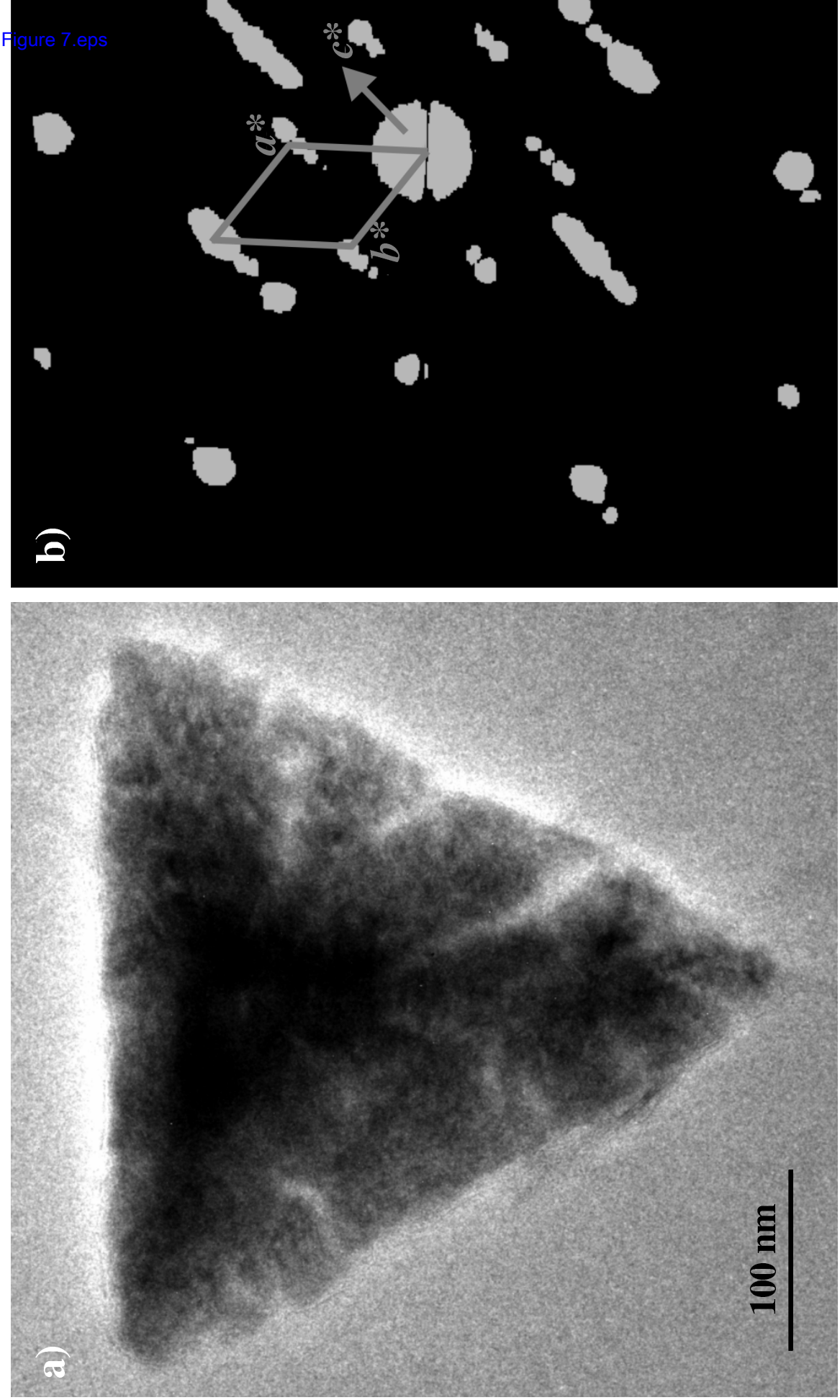


Figure 8
Click here to download Figure: Figure 8.eps

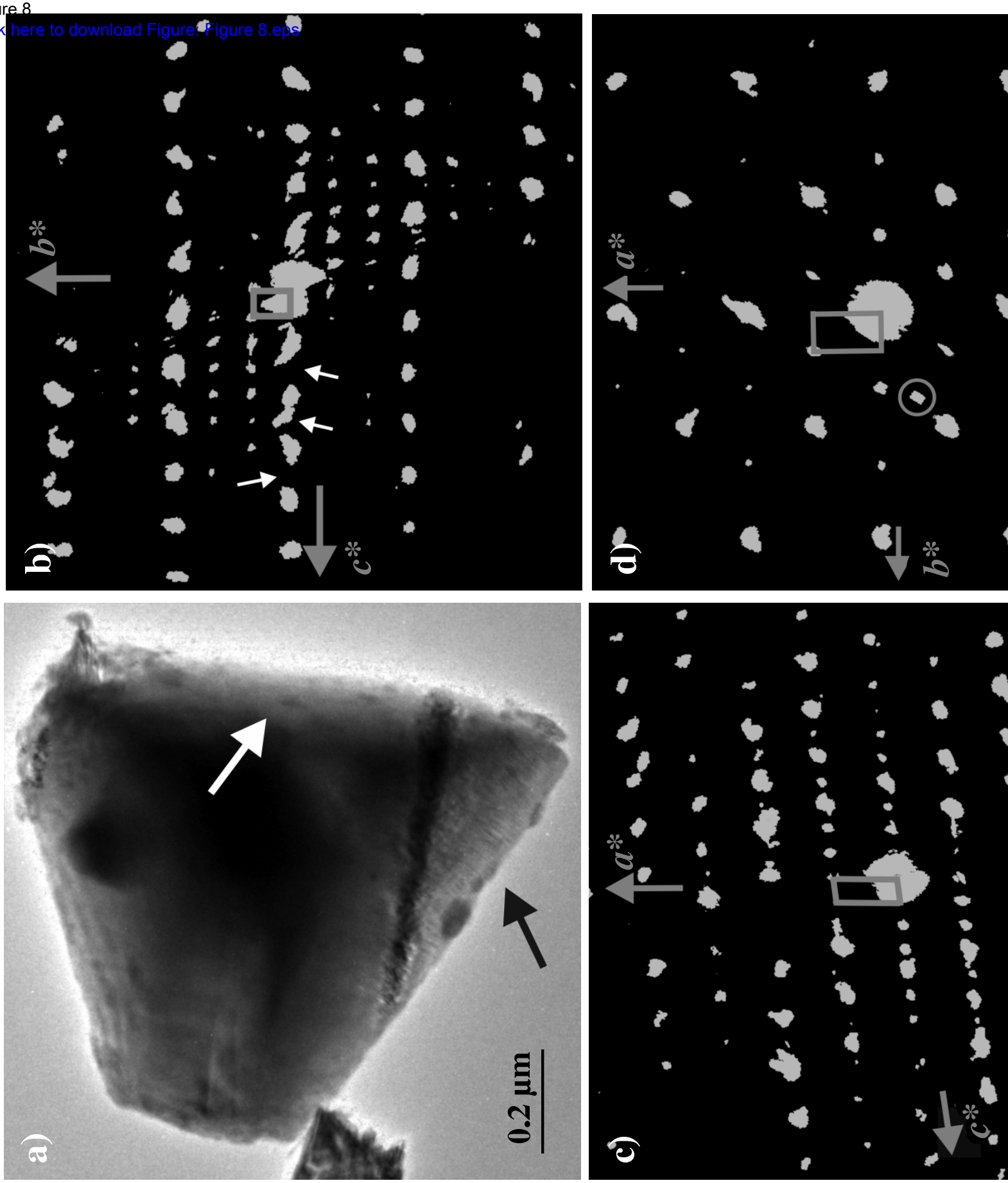
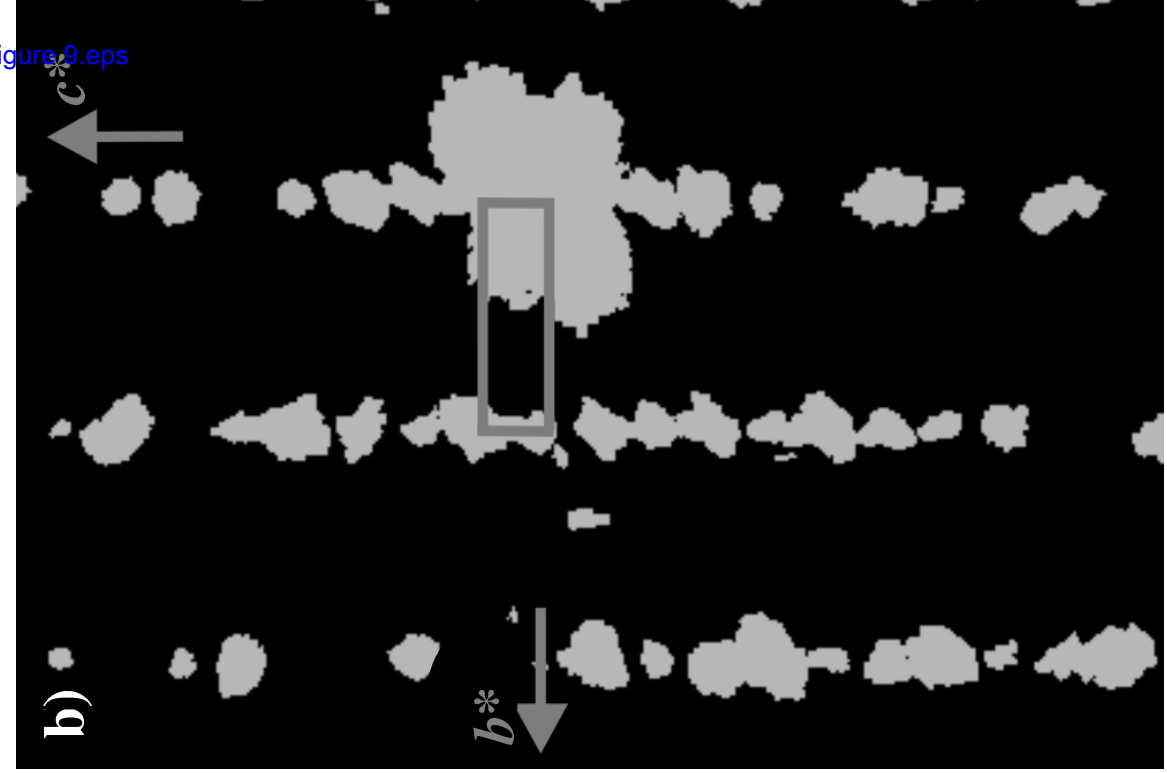


Figure 9
Click here to download Figure: Figure 9.eps



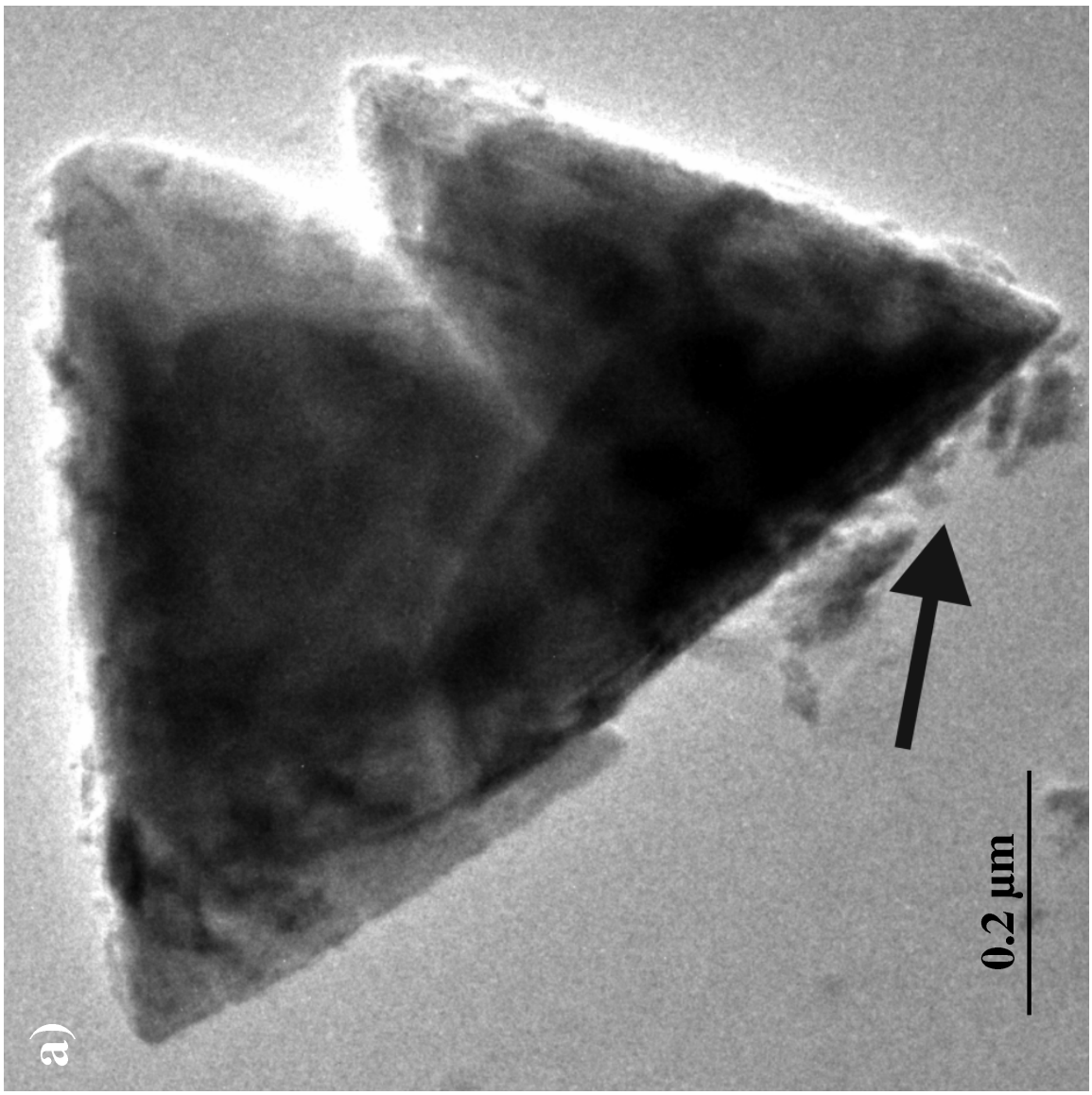


Figure 10
Click here to download Figure: Figure 10.eps

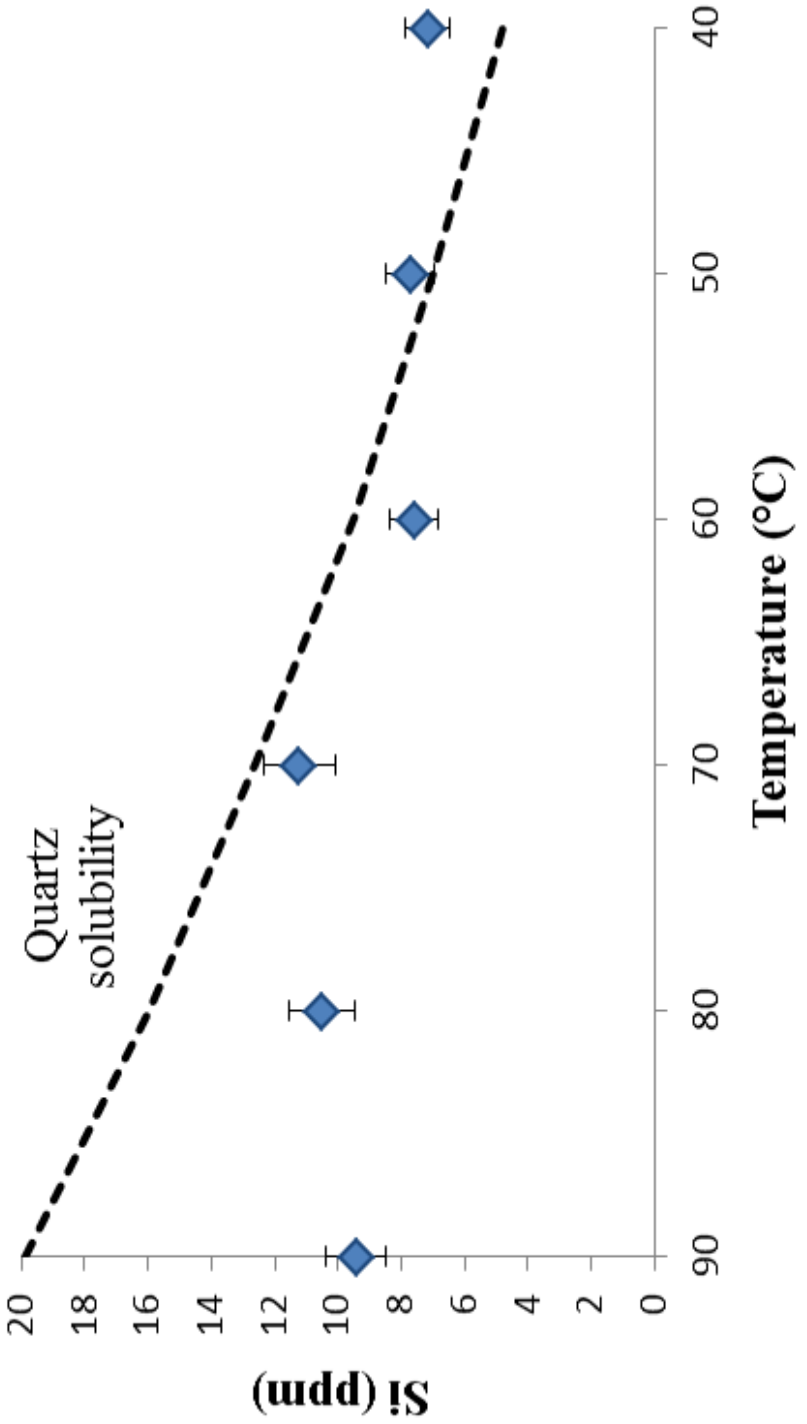


Figure 11
Click here to download Figure: Figure 11.eps

